Two competing soft modes and an unusual phase transition in the stuffed tridymite-type oxide $BaAl_2O_4$

Y. Ishii,[1,*] S. Mori,[1] Y. Nakahira,[2] C. Moriyoshi,[2] J. Park,[3] B. G. Kim,[3] H. Moriwake,[4] H. Taniguchi,[5] and Y. Kuroiwa[2]

[1]*Department of Materials Science, Osaka Prefecture University, Sakai, Osaka 599-8531, Japan*

[2]*Department of Physical Science, Hiroshima University, Higashihiroshima, Hiroshima 739-8526, Japan*

[3]*Department of Physics, Pusan National University, Pusan 609-735, South Korea*

[4]*Japan Fine Ceramics Center, Nagoya 456-8587, Japan*

[5]*Department of Physics, Nagoya University, Nagoya 464-8602, Japan*

(Received 10 October 2015; revised manuscript received 25 March 2016; published 18 April 2016)

We investigated the structural phase transition of $BaAl_2O_4$, which has a network structure with corner-sharing AlO_4 tetrahedra, via synchrotron x-ray thermal diffuse scattering measurements and first-principles calculations. $BaAl_2O_4$ shows the structural phase transition at $T_C = 451.4$ K from the $P6_322$ parent crystal structure to the low-temperature superstructure with a cell volume of $2a \times 2b \times c$. This phase transition is unusual, in which two energetically competing phonon modes at M and K points soften simultaneously. When approaching T_C from above, the K-point mode appears first. However, this K-point mode is overcome by the later-developed M-point mode. The thermal diffuse scattering intensities from both modes increase sharply at T_C; therefore, both modes soften simultaneously. The first-principles calculations demonstrate that the M-point mode is electrostatically more preferable than the K-point mode and determines the eventual low-temperature structure, although these two modes are competing energetically. This competition is characteristic of $BaAl_2O_4$, which is ascribed to the structurally flexible network structure of this compound.

DOI: 10.1103/PhysRevB.93.134108

I. INTRODUCTION

Phonon softening, such as that in charge density waves (CDWs) [1–4], is one of the recent central issues in solid-state physics, although it has been extensively studied for decades. Conventionally, a structural phase transition associated with soft phonons is driven by a particular soft phonon, in which the frequency of a single soft mode decreases on cooling and eventually reaches zero at a transition temperature. Here, a structural phase transition driven by more than one soft mode is investigated.

In compounds with a corner-sharing tetrahedral network structure, e.g., tridymite and quartz which are SiO_2 modifications, characteristic diffuse scatterings have been observed in electron diffraction patterns [5–7], which are ascribed to particular phonon modes called rigid unit modes (RUMs) [5,8]. These modes are associated with the rotation or tilting of each tetrahedral block without distortion of the bonding between the corner ligand and center atom [9,10]. The distortion energy caused by these phonon modes is so small that the structure is likely to fluctuate. The RUM is known to occasionally act as a soft mode. For example, nepheline, one of the derivatives of the tridymite-type structure, exhibits a structural phase transition accompanying a soft mode, which is characterized as a RUM [11].

We highlighted a network compound, $BaAl_2O_4$, which exhibits structural fluctuations over a wide temperature range. This compound crystallizes in a stuffed tridymite-type structure that comprises a corner-sharing, AlO_4 tetrahedral network with occupied six-member cavities. The crystal structure is chiral and noncentrosymmetric. The high-temperature phase with a space-group symmetry of $P6_322$ undergoes a structural phase transition at approximately 400 K, accompanying the significant tilting of the AlO_4 tetrahedra [12–14]. This results in the doubling of the cell parameters in the a and b axes, and the low-temperature phase with $P6_3$ space group exhibits a small spontaneous polarization. This transition has been characterized as an improper-type ferroelectric phase transition [15].

RUMs have also been investigated in $BaAl_2O_4$ through *ab initio* calculations. According to previous studies by Perez-Mato *et al.*, an unstable RUM in an AlO_4 tetrahedral framework plays an important role in the dominant structural instability of this compound [16]. In the electron diffraction for the high-temperature phase of $BaAl_2O_4$, characteristic honeycomblike diffuse streaks along three equivalent ⟨110⟩ reciprocal directions have been observed [17]. Because the diffuse scattering intensity is strongly dependent on the temperature, it is anticipated that this characteristic diffuse streak pattern may stem from a soft mode. A similar diffuse pattern has also been observed for $Ba_{0.6}Sr_{0.4}Al_2O_4$ polycrystalline samples [18]. According to the structure refinements and maximum-entropy method (MEM) analyses, three-site disorder exists at the bridging oxygen atoms, thus indicating that the structural phase transition of $BaAl_2O_4$ is of an order-disorder type.

In the present study, we investigated the structural phase transition of $BaAl_2O_4$ by means of synchrotron x-ray thermal diffuse scatterings (TDS). While the neutron and x-ray inelastic scatterings are traditional for studying phonon dispersion and its dynamics, the TDS measurement has recently become well established [19–21] and is a useful method for a wide range of material sciences. By utilizing the TDS, we demonstrate that the framework compound $BaAl_2O_4$ is an example in which two distinct phonon modes soften at T_C simultaneously.

*ishii@mtr.osakafu-u.ac.jp

II. EXPERIMENT

Single crystals of $BaAl_2O_4$ were grown by the self-flux method. Previously prepared $BaAl_2O_4$ and $BaCO_3$ powders were mixed at a molar ratio of 50:17. The preparation method of $BaAl_2O_4$ powder can be found in Ref. [22]. The mixture was placed in a platinum crucible. After heating at 1470 °C for 6 h, the crucible was slowly cooled to 1200 °C at a rate of 2 °C/h, then cooled in a furnace to room temperature. The shiny, colorless crystals had hexagonal shape edges of approximately 100 μm long and were mechanically separated from the flux. Synchrotron x-ray diffraction experiments at 300–800 K were performed at the BL02B1 beam line of SPring-8 [23]. The incident x-ray radiation was set at 25 keV. The diffraction intensities were recorded on a large cylindrical image-plate camera. The temperature control was performed using N_2 gas flow.

First-principles calculations were performed using the projector augmented-wave (PAW) method [24] within the framework of density functional theory (DFT) [25,26], as implemented in VASP code [27,28]. Exchange-correlation interactions were treated by the generalized gradient approximation (GGA) [29]. Lattice constants and internal coordinates were optimized by lowering the residual Hellmann-Feynman forces less than 1.0×10^{-3} eV/Å. Phonon-dispersion calculations were performed using the PHONON code and PHONOPY [30,31].

III. RESULTS AND DISCUSSION

Figure 1(a) shows the diffraction pattern near the $11\underline{10}$ and $\bar{1}2\underline{10}$ fundamental peaks obtained at 500 K. Thermal diffuse scatterings are observed along $[\bar{2}10]$, which is one of the three equivalent $\langle 110 \rangle$ directions. This direction corresponds to $\Gamma' - K' - M - K - \Gamma''$ in the reciprocal space, as shown in Fig. 1(b). The intensities of these diffuse scatterings are strongly dependent on the temperature, as reported in Ref. [17], and exist at all temperatures used for the measurements. In addition, cross-shaped thermal diffuse scatterings are observed around each fundamental peak, although the intensities of these diffuse scatterings are largely independent of the temperature and are present at all temperatures used for the measurements.

We investigated the temperature dependence of the diffuse scatterings between two fundamental peaks. Figure 1(c) shows the intensity obtained at typical temperatures at $(1-2\eta, 1+\eta, 10)$, in which $\eta = 0$ and $\eta = 1$ correspond to the (1,1,10) and $(\bar{1},2,10)$ reciprocal points, respectively. All of the profiles obtained at various temperatures between 300 and 800 K are shown in the Supplemental Material [32] as Figs. S2 and S3. The intensities were normalized using the $11\underline{10}$ fundamental peak at each temperature. The intensities below $\eta = 0.2$ and above $\eta = 0.8$ come from the $11\underline{10}$ and $\bar{1}2\underline{10}$ fundamental peaks. These diffuse scatterings within $0.2 < \eta < 0.8$ can be satisfactorily fitted using several Gaussian functions. The red line shows the superposition of these fitting curves. For fitting below 445 K, the strong superlattice reflections were subtracted from each profile.

At 600 K, there are two broad diffuse peaks near $\eta = \pm 1/3$, as indicated by the green arrows. Similar peaks are also observed at 700 and 800 K. In addition to these two diffuse peaks, another broad diffuse peak can be seen near $\eta = 1/2$ at 500 K, as indicated by the gray arrow. At 455.2 K, an additional small peak appears at $\eta = 1/2$, as indicated by the blue arrow. This small peak develops as a superlattice reflection at low temperature. These diffuse scatterings near $\eta = 1/2$ and $\pm 1/3$ exist at all temperatures used for the measurements. The small peak at $\eta = 1/2$ at 455.2 K, indicated by the blue arrow in Fig. 1(c), can be understood as the short-range ordering of the $2a \times 2b \times c$ superstructure. There is no apparent difference for these features when approaching T_C from above and below.

Figure 2 shows the maximum intensity and full width at half maximum (FWHM) of the superlattice reflections as a function of temperature. The small peaks such as those observed at 455.2 K in Fig. 1(c) are also included. The inset shows the square root of the superlattice intensity, $(I/I_0)^{1/2}$, and the FWHM in the range of T = 430–470 K. The superlattice

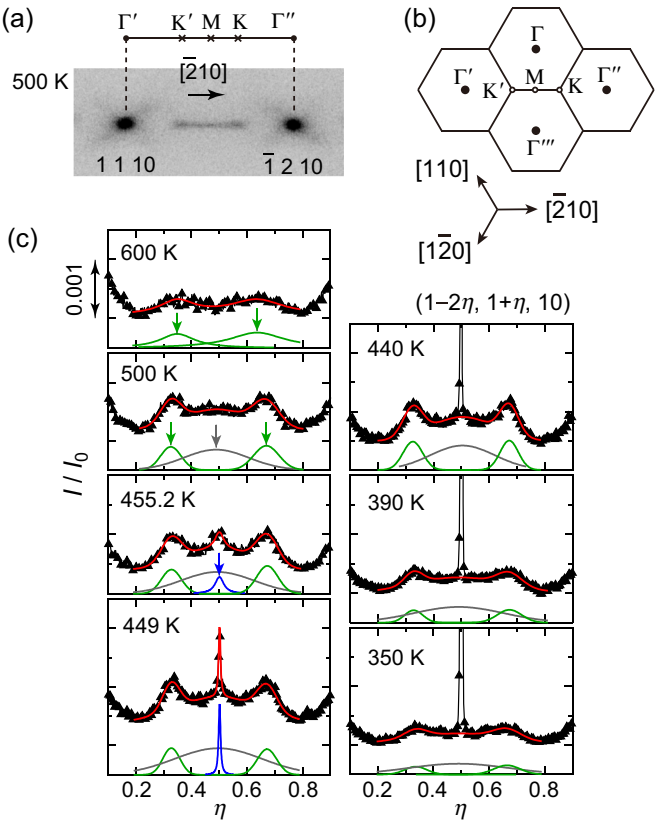

FIG. 1. (a) Typical diffraction pattern near the $11\underline{10}$ and $\bar{1}2\underline{10}$ fundamental peaks recorded on the image-plate camera at 500 K. (b) Cross-sectional reciprocal space (h, k, 0) of a primitive hexagonal lattice. The symmetric points are also shown. (c) Intensities from the $11\underline{10}$ to $\bar{1}2\underline{10}$ fundamental peaks at 350–600 K. All profiles are drawn using the same scale. The intensities were normalized using the maximum intensity of the $11\underline{10}$ fundamental peak at each temperature. They are fitted using several Gaussian functions shown by green, gray, and blue lines. The red lines are the superposition of these Gaussian functions. For the fitting below 445 K, the superlattice reflections have been subtracted. The green arrows indicate the peak positions of diffuse scatterings of the K-point mode. Gray and blue arrows indicate the peak positions of the broad diffuse scattering of the M-point mode and the superlattice reflection, respectively. Data were collected upon heating.

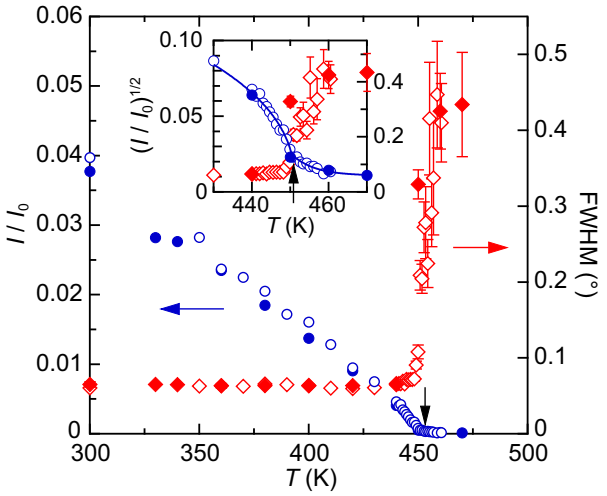

FIG. 2. Normalized maximum superlattice intensity (left axis) and FWHM (right axis) plotted against temperature. The open and closed symbols represent the data obtained upon heating and cooling, respectively. The standard deviations of the normalized intensity data were considerably smaller than the marker size. The inset shows the square root of the superlattice intensity (left axis) and FWHM (right axis) near T_C. T_C is indicated by arrows in each figure. The solid lines are the fits using a power law ($T < T_C$) and an exponential function ($T > T_C$).

intensity decreases with increasing temperature. It shows a kink at approximately 450 K, as indicated by the arrows in the figures. Above ~450 K, the weak intensity still exists as a tail, and the FWHM increases abruptly with increasing temperature. A similar tail behavior has also been observed in $BaMnF_4$, with high concentrations of defects [33,34], and manganese compounds [35–37]. Below ~450 K, the long-range ordering of the $2a \times 2b \times c$ superstructure appears. Therefore, it is reasonable to regard this temperature as T_C. The $(I/I_0)^{1/2}$ values shown in the inset were fitted using a power function and exponential function. The curve below T_C was fitted using a power function, $A_0(T_C - T)^{\beta}$, where $\beta = 0.40$ and $T_C = 451.4$. A_0 is a coefficient. The obtained critical index β coincides well with the theoretical value of the order-disorder type [38]. An exponential function was found to accurately reproduce the tail part above T_C.

Figures 3(a)–3(h) display the temperature dependence of the intensities, peak positions (η_{peak}), FWHMs, and the correlation length (ξ) of the thermal diffuse scatterings near $\eta = 1/2$ and $\pm 1/3$. The scattering intensities of both diffuse scatterings increase sharply at T_C, as shown in Figs. 3(a) and 3(e). This result means that these diffuse scatterings stem from phonon modes, and both modes soften at T_C simultaneously. As described later, these diffuse peaks near $\eta = 1/2$ and $\pm 1/3$ can be attributed to the soft modes at the M and K points, respectively. Because the diffuse peak of the M-point mode is sufficiently broad, the η_{peak} of the M-point mode is difficult to determine with high accuracy, as shown in Fig. 3(b). It is reasonable to consider that the η_{peak} of the M-point mode has a commensurate value, $\eta = 1/2$. The peak positions of the superlattice reflections are also plotted in Fig. 3(b). The superlattice reflections are at the commensurate position. In contrast, the η_{peak} for the diffuse peak near $\eta = 1/3$ shows an

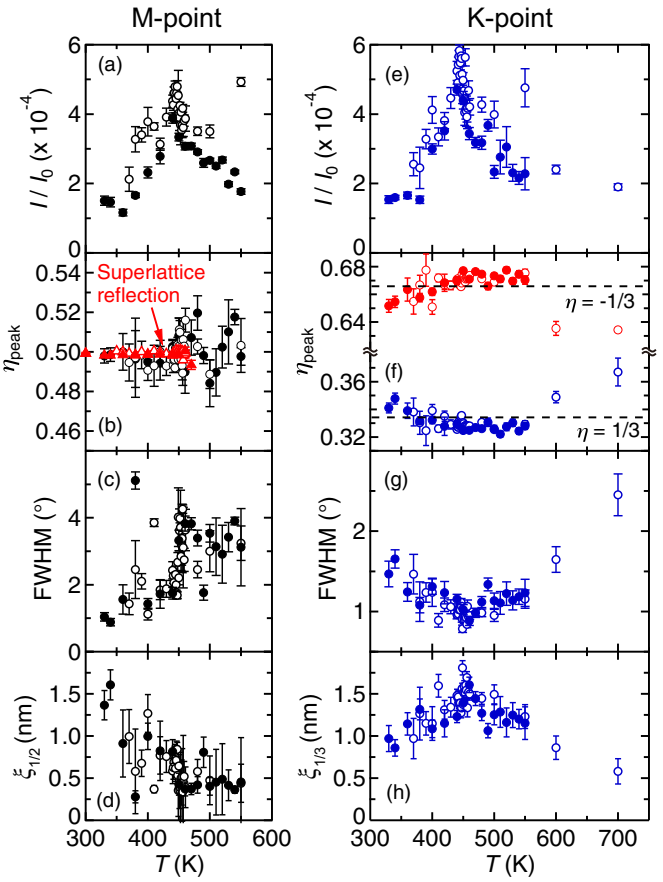

FIG. 3. Normalized maximum intensity, peak position (η_{peak}), FWHM, and correlation length (ξ) of the thermal diffuse scatterings near $\eta = 1/2$ and $1/3$, which correspond to the soft modes at the M point and K point, respectively. (a)–(d) and (e)–(h) correspond to the thermal diffuse scatterings of the M- and K-point modes, respectively. The peak positions of the superlattice reflections and the thermal diffuse peaks near $\eta = -1/3$ are also plotted in (b) and (f), respectively. The open and closed symbols represent the data obtained upon heating and cooling, respectively.

intriguing behavior, as shown in Fig. 3(f); namely, η_{peak}~0.36 above 600 K, $\eta_{peak} \sim 0.32$ at $T_C < T < 550$ K, and then it shifts toward 1/2 below T_C. Neither η_{peak} above T_C nor below T_C show the commensurate values. Similar results were obtained for the diffuse peak near $\eta = -1/3$. The FWHMs of the diffuse peaks are plotted in Figs. 3(c) and 3(g), respectively. The FWHM of the M-point diffuse peak abruptly decreases at T_C as the superlattice develops. Correspondingly, the $\xi_{1/2}$ develops below T_C. In contrast, the FWHM of the K-point diffuse peak decreases gradually with decreasing temperature, showing a minimum at T_C, and then increases below T_C. Consequently, $\xi_{1/3}$ exhibits a maximum at T_C, as shown in Fig. 3(h). These behaviors are also observed on heating.

The results shown in Figs. 3 indicate that these two soft modes at the M and K points coexist and compete above T_C. In the high-temperature phase, the K-point mode has already appeared above 600 K, as shown in Fig. 3(e), whereas the M-point mode appears at 550 K. Moreover, the K-point mode exhibits a stronger intensity and longer $\xi_{1/3}$ than the M-point mode. Nevertheless, the M-point mode is selected to form the

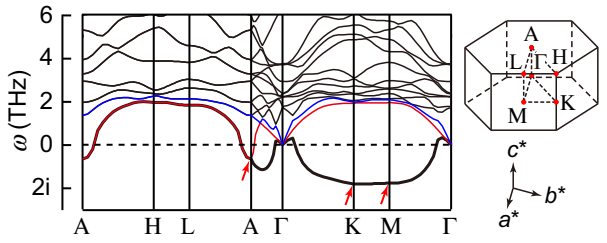

FIG. 4. Phonon-dispersion curves of $BaAl_2O_4$ obtained by first-principles calculations. The calculations were performed on the $P6_322$ parent structure. The inset shows the first Brillouin zone of a primitive hexagonal lattice. Three acoustic phonon branches are shown as red, blue, and thick black lines. One of the acoustic phonon branches shows imaginary frequencies at the *A*, *K*, and *M* points, as indicated by red arrows.

superstructure below T_C, and the *K*-point mode is overcome by the later-developed *M*-point mode. In this unusual structural phase transition, the soft phonon fluctuates between the *M* point and *K* point, that is, "fluctuation in phonons" in the *k* space. These two soft modes have also been reported in $Ba_{1-x}Sr_xAl_2O_4$ recently [39].

We investigated the phonon dispersions via first-principles calculations. The calculated phonon dispersion of $BaAl_2O_4$ is shown in Fig. 4. We found one of the acoustic phonon branches showing the imaginary frequencies at the *A*, *K*, and *M* points, which indicates the structural instability giving rise to the structural phase transition. The calculated imaginary frequencies were 0.67, 1.77, and 1.80 THz at the *A*, *K*, and *M* points, respectively. The structural instabilities at the *M* and *K* points are larger than that at the *A* point. These two structural instabilities cause the *M*- and *K*-point soft modes. The calculation also reveals that the difference in the destabilization energy at the *M* and *K* points is quite small.

The obtained vibration patterns at the *M* and *K* points are shown in Fig. 5. The vibration displacements for each atom are listed in Table I. We also attached the animation files showing the vibration patterns at the *M* and *K* points (see Supplemental Material [32] for 2phonon-m-c.avi and phonon-m-c-441.avi for the *M*-point mode, and 2phonon-k-c.avi and phonon-k-c-441.avi for the *K*-point mode). The vibration patterns of oxygen atoms are predominantly arranged along the *c* axis except for O1 and O2 atoms, which are the bridging atoms of two AlO_4 tetrahedrons (see Fig. 5). The vibrations of bridging O atoms are found in the *ab* plane. In both modes, the *a*- and *b*-axis vibration of the bridging O atoms is $\pi/2$ out of phase. Therefore, the bridging O atoms show circular motion.

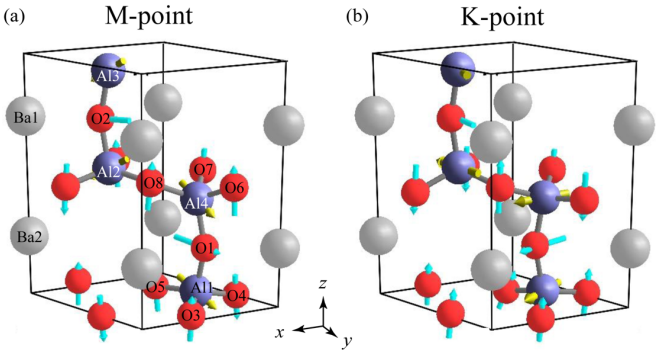

FIG. 5. Vibration patterns of imaginary-frequency component at the (a) *M* and (b) *K* points for each atom in a primitive cell of the parent $P6_322$ structure. Ba, Al, and O atoms are indicated by a gray, blue, and red ball, respectively. Arrows show the direction of vibration for each atom. The calculations were performed for a $3 \times 3 \times 2$ supercell.

TABLE I. Vibration displacement at the *M* and *K* points for each atom in a primitive cell of $P6_322$ phase. Displacement is composed of a complex number to indicate vibration phase and amplitude.

Atom	Vibration displacement					
	Real part			Imaginary part		
	a	*b*	*c*	*a*	*b*	*c*
M point (Å)						
Ba1	0.001	−0.002	0.004	0.000	0.000	0.000
Ba2	−0.001	0.002	0.004	0.000	0.000	0.000
Al1	−0.006	0.008	−0.006	0.010	−0.014	0.011
Al2	0.006	−0.008	−0.006	0.010	−0.014	−0.011
Al3	0.004	−0.009	−0.006	0.007	−0.016	−0.011
Al4	−0.004	0.009	−0.006	0.007	−0.016	0.011
O1	−0.032	0.056	−0.006	0.056	−0.097	0.011
O2	0.032	−0.056	−0.006	0.056	−0.097	−0.011
O3	0.000	0.003	0.033	0.000	0.006	0.064
O4	−0.003	−0.002	−0.043	0.000	0.000	0.000
O5	0.003	−0.001	0.033	−0.005	0.003	−0.064
O6	0.000	−0.003	0.033	0.000	0.006	−0.064
O7	0.003	0.002	−0.043	0.000	0.000	0.000
O8	−0.003	0.001	0.033	−0.005	0.003	0.064
K point (Å)						
Ba1	0.000	0.000	0.006	0.000	0.000	−0.005
Ba2	0.000	0.000	0.006	0.000	0.000	−0.005
Al1	0.014	0.010	0.000	0.010	−0.014	0.000
Al2	0.007	−0.015	0.000	0.015	0.007	0.000
Al3	−0.001	−0.017	0.000	0.017	−0.001	0.000
Al4	0.016	0.001	0.000	0.001	−0.017	0.000
O1	0.087	0.030	0.000	0.030	−0.087	0.000
O2	0.017	−0.091	0.000	0.091	0.017	0.000
O3	0.000	0.008	0.042	0.000	−0.004	0.046
O4	−0.007	−0.004	0.042	0.003	0.002	0.046
O5	−0.007	0.004	0.012	−0.004	0.002	−0.060
O6	0.000	−0.005	−0.039	0.000	0.008	−0.048
O7	0.004	0.002	−0.039	−0.007	−0.004	−0.048
O8	−0.003	0.002	0.062	−0.007	0.004	−0.004

Based on these calculation results, the following considerations can be given. First, according to our calculations, both the *M*- and *K*-point modes include the tilting of AlO_4 tetrahedra, as shown in Fig. 5 and the animation files (see Supplemental Material [32]). In other words, both modes can be associated with the tilting of AlO_4 tetrahedra, which are related to the previously reported RUMs [16]. In addition, the crystal structure of $BaAl_2O_4$ is quite gappy and spatially flexible owing to the AlO_4 network structure. These situations happen to allow this compound to possess the competing two modes. In this point of view, $BaAl_2O_4$ is exceptional and unique among the compounds with a polyhedral network.

Second, as can be seen in the animation files (see Supplemental Material [32]), the distortion caused by the *K*-point

mode induces a considerable Coulomb repulsion between the bridging O atoms and the basal O atoms; the basal O atoms move toward the bridging O atoms, which causes a too much shorter distance between the bridging O atoms and the basal O atoms. This mode is electrostatically unfavorable. On the other hand, the vibration pattern at the M point relieves this Coulomb repulsion by avoiding the bridging atoms to get close to the basal O atoms. Therefore, the M-point mode is electrostatically more preferable when the structural phase transition happens. The previously reported threefold superstructure in $Ba(Al,Fe)_2O_4$ [40] is probably caused by a slight modification in the structural stability owing to the Al-site disorder.

The dispersion showing the structural instabilities is characterized as one of the transverse acoustic modes, which degenerates at the Brillouin zone boundary of $k_z = \pi/c$. This degeneracy is lifted at $k_z = 0$. The longitudinal acoustic mode is indicated by the blue line in Fig. 4. Because the diffuse scattering intensity is proportional to $|\boldsymbol{K} \cdot \boldsymbol{e}_{j,q}|/\omega_q^2$, where $\boldsymbol{K}$, $\boldsymbol{e}_{j,q}$, and ω_q are the scattering vector, atomic displacement unit vector of the j atom, and the phonon frequency, respectively, the scattering intensity by the transverse soft mode with $\boldsymbol{q}//[110]$ is expected to disappear along $\boldsymbol{K}//[110]$. This is evidenced by the transmission electron microscope (TEM) experiments, as shown in Fig. S4 of the Supplemental Material [32].

Recently observed intriguing phenomena, such as unconventional superconductivity [41,42], multiferroics [43–45], and spin Hall effect [46], are closely related to the inversion symmetry breaking of crystal structures. Fundamental understandings of phonon modes during the structural phase transition of such a crystal without inversion center are very important to design these emergent functionalities. In addition, the ferroelectric transition in $BaAl_2O_4$ is of an improper type, which is essential to multiferroics. We believe that the finding of the simultaneous softening of the two distinct phonon modes in noncentrosymmetric and chiral $BaAl_2O_4$ will be significantly important for further developments of these novel functionalities.

IV. CONCLUSION

$BaAl_2O_4$ is a rare compound that shows the unusual structural phase transition associated with two unstable phonon modes. Its high-temperature phase has energetically competing, unstable phonon modes at the M and K points. Both modes soften simultaneously at T_C, which results in the sharp increase in the thermal diffuse scattering intensities at the M and K points. Because the K-point mode is electrostatically unfavorable, the M-point mode determines the eventual crystal structure of the low-temperature phase. This is characteristic in $BaAl_2O_4$ and can be attributed to the corner-sharing AlO_4 network structure in this compound.

ACKNOWLEDGMENTS

This work was partly supported by a Grant-in-Aid for Scientific Research from the Ministry of Education, Culture, Sports, Science and Technology of Japan (MEXT), MEXT Element Strategy Initiative Project, Grant-in-Aid for Challenging Exploratory Research (Grant No. 15K14120), and Grant-in-Aid for Scientific Research on Innovative Areas "Nano Informatics" (Grant No. 25106008) from the Japan Society for the Promotion of Science (JSPS). This study was also partly supported by the NSF of Korea (Grant No. NSF-2015R1D1A1A01057589). The computational resources were provided by the KISTI Supercomputing Center (Project No. KSC-2015-C1-007). The experiments at SPring-8 were performed with the approval of the Japan Synchrotron Radiation Research Institute (JASRI; Proposals No. 2014A0078, No. 2014A1323, No. 2014B0078, and No. 2015A1507).

[1] Y. I. Joe, X. M. Chen, P. Ghaemi, K. D. Finkelstein, G. A. de la Peña, Y. Gan, J. C. T. Lee, S. Yuan, J. Geck, G. J. MacDougall, T. C. Chiang, S. L. Cooper, E. Fradkin, and P. Abbamonte, Nat. Phys. **10**, 421 (2014).

[2] Y. Yamada, K. Kitsuda, S. Nohdo, and N. Ikeda, Phys. Rev. B **62**, 12167 (2000).

[3] E. Morosan, H. W. Zandbergen, B. S. Dennis, J. W. G. Bos, Y. Onose, T. Klimczuk, A. P. Ramirez, N. P. Ong, and R. J. Cava, Nat. Phys. **2**, 544 (2006).

[4] B. Sipos, A. F. Kusmartseva, A. Akrap, H. Berger, L. Forrò, and E. Tutiš, Nat. Mater. **7**, 960 (2008).

[5] M. T. Dove, K. D. Hammonds, V. Heine, R. L. Withers, X. Xiao, and R. J. Kirkpatrick, Phys. Chem. Miner. **23**, 56 (1996).

[6] R. L. Withers, J. G. Thompson, Y. Xiao, and R. J. Kirkpatrick, Phys. Chem. Miner. **21**, 421 (1994).

[7] H. Arnold, Z. Kristallogr. **121**, 145 (1965).

[8] B. Berge, J. P. Bachheimer, G. Dolino, M. Vallade, and C. M. E. Zeyen, Ferroelectrics **66**, 73 (1986).

[9] M. T. Dove, A. P. Giddy, and V. Heine, Trans. Am. Crystallogr. Assoc. **27**, 65 (1993).

[10] K. D. Hammonds, M. T. Dove, A. P. Giddy, V. Heine, and B. Winkler, Am. Mineral. **81**, 1057 (1996).

[11] S. A. Hayward, A. K. A. Pryde, R. F. de Dombal, M. A. Carpenter, and M. T. Dove, Phys. Chem. Miner. **27**, 285 (2000).

[12] S.-Y. Huang, R. V. D. Mühll, J. Ravez, and M. Couzi, Ferroelectrics **159**, 127 (1994).

[13] S.-Y. Huang, R. V. D. Mühll, J. Ravez, J. P. Chaminade, P. Hagenmuller, and M. Couzi, J. Solid State Chem. **109**, 97 (1994).

[14] A.-K. Larsson, R. L. Withers, J. M. Perez-Mato, J. D. F. Gerald, P. J. Saines, B. J. Kennedy, and Y. Liu, J. Solid State Chem. **181**, 1816 (2008).

[15] H. T. Stokes, C. Sadate, D. M. Hatch, L. L. Boyer, and M. J. Mehl, Phys. Rev. B **65**, 064105 (2002).

[16] J. M. Perez-Mato, R. L. Withers, A.-K. Larsson, D. Orobengoa, and Y. Liu, Phys. Rev. B **79**, 064111 (2009).

[17] A. M. Abakumov, O. I. Lebedev, L. Nistor, G. V. Tendeloo, and S. Amelinckx, Phase Trans. **71**, 143 (2000).

[18] K. Fukuda, T. Iwata, and T. Orito, J. Solid State Chem. **178**, 3662 (2000).

[19] M. Holt, Z. Wu, H. Hong, P. Zschack, P. Jemian, J. Tischler, H. Chen, and T.-C. Chiang, Phys. Rev. Lett. **83**, 3317 (1999);

M. Y. Chou and M. Choi, *ibid.* **84**, 3733 (2000); M. Holt and T.-C. Chiang, *ibid.* **84**, 3734 (2000).
[20] M. Holt, P. Zschack, H. Hong, M. Y. Chou, and T.-C. Chiang, Phys. Rev. Lett. **86**, 3799 (2001).
[21] R. Xu, H. Hong, P. Zschack, and T.-C. Chiang, Phys. Rev. Lett. **101**, 085504 (2008).
[22] E. Tanaka, Y. Ishii, H. Tsukasaki, H. Taniguchi, and S. Mori, Jpn. J. Appl. Phys. **53**, 09PB01 (2014).
[23] K. Sugimoto, H. Ohsumi, S. Aoyagi, E. Nishibori, C. Moriyoshi, Y. Kuroiwa, H. Sawa, and M. Takata, AIP Conf. Proc. **1234**, 887 (2010).
[24] P. E. Blöchl, Phys. Rev. B **50**, 17953 (1994).
[25] P. Hohenberg and W. Kohn, Phys. Rev. **136**, B864 (1964).
[26] W. Kohn and Sham, Phys. Rev. **140**, A1133 (1965).
[27] G. Kresse and J. Furthmüller, Phys. Rev. B **54**, 11169 (1996).
[28] G. Kresse and D. Joubert, Phys. Rev. B **59**, 1758 (1999).
[29] J. P. Perdew, K. Burke, and M. Ernzerhof, Phys. Rev. Lett. **77**, 3865 (1996).
[30] K. Parlinski, Y. Kawazoe, and Y. Waseda, J. Chem. Phys. **114**, 2395 (2001).
[31] A. Togo and I. Tanaka, Scr. Mater. **108**, 1 (2015).
[32] See Supplemental Material at http://link.aps.org/supplemental/10.1103/PhysRevB.93.134108 for the details of the XRD data, the phonon vibration movies, and the TEM observation results.
[33] T. W. Ryan, R. A. Cowley, and S. R. Andrews, J. Phys. C **19**, L113 (1986).
[34] D. E. Cox, S. M. Shapiro, R. J. Nelmes, T. W. Ryan, H. J. Bleif and R. A. Cowley, M. Eibschutz, and H. J. Guggenheim, Phys. Rev. B **28**, 1640 (1983).
[35] S. Shimomura, T. Tonegawa, K. Tajima, N. Wakabayashi, N. Ikeda, T. Shobu, Y. Noda, Y. Tomioka, and Y. Tokura, Phys. Rev. B **62**, 3875 (2000).
[36] S. Shimomura, N. Wakabayashi, H. Kuwahara, and Y. Tokura, Phys. Rev. Lett. **83**, 4389 (1999).
[37] S. Shimomura, K. Torashima, N. Wakabayashi, K. Nishimoto, T. Tonegawa, N. Hayama, H. Sawa, Y. Tomioka, and Y. Tokura, J. Phys. Soc. Jpn. **76**, 124603 (2007).
[38] W. Gebhardt and U. Krey, *Phasenübergänge und Kritische Phänomene* (Friedr. Vieweg & Sohn, Braunschweig/Wiesbaden, 1980).
[39] Y. Ishii, H. Tsukasaki, E. Tanaka, and S. Mori, Sci. Rep. **6**, 19154 (2016).
[40] S. Mori, S. Katsumura, T. Ozaki, E. Tanaka, Y. Ishii, K. Kurushima, Y. Kubota, and H. Taniguchi, Ferroelectrics **464**, 116 (2014).
[41] F. Kneidinger, E. Bauer, I. Zeiringer, P. Rogl, C. Blaas-Schenner, D. Reith, and R. Podloucky, Physica C **514**, 388 (2015).
[42] S. Yip, Annu. Rev. Condens. Matter Phys. **5**, 15 (2014).
[43] T. Kimura, T. Goto, H. Shintani, K. Ishizuka, T. Arima, and Y. Tokura, Nature (London) **426**, 55 (2003).
[44] W. Eerenstein, N. S. Mathur, and J. F. Scott, Nature (London) **442**, 759 (2006).
[45] C. Pfleiderer, A. Neubauer, S. Mühlbauer, F. Jonietz, M. Janoschek, S. Legl, R. Ritz, W. Münzer, C. Franz, P. G. Niklowitz, T. Keller, R. Georgii, P. Böni, B. Binz, and A. Rosch, J. Phys.: Condens. Matter **21**, 279801 (2009).
[46] J. Sinova, D. Culcer, Q. Niu, N. A. Sinitsyn, T. Jungwirth, and A. H. MacDonald, Phys. Rev. Lett. **92**, 126603 (2004).